International Journal of Precision Engineering and Manufacturing-Green Technology (2026) 13:1881–1891
https://doi.org/10.1007/s40684-026-00847-z

Online ISSN 2198-0810
Print ISSN 2288-6206

REGULAR PAPER

Rowing Machine Integrated Multifunctional Triboelectric Nanogenerator for Exercise Motion Energy Harvesting

Jaeung Choi[1] · Seh-Hoon Chung[1] · Deokjae Heo[2] · Sunghan Kim[1] · Jinkee Hong[3] · Sangmin Lee[1]

Received: 14 August 2025 / Revised: 26 December 2025 / Accepted: 11 January 2026 / Published online: 11 February 2026
© The Author(s) 2026

Abstract

Triboelectric nanogenerators (TENGs) have been studied in various fields because of their ease of fabrication, simple structures, and diverse material choices. Therefore, integrating TENGs into various systems has become a key research focus. However, simply integrating TENGs into systems limits their practical use because of their high design complexity and low output. To overcome this, a design strategy supporting the primary system functions is required. In this study, we focused on a rowing-machine-integrated triboelectric nanogenerator (RM-TENG) with controllable mechanical resistance. To minimize wear during high-speed rotation, the dielectric and nickel electrode films were designed to brush lightly against the aluminum electrode. This contact enabled electrostatic discharge during sliding and enhanced the voltage and current outputs to 440 V and 1.16 A, respectively. The mechanical resistance and electrical signal could be adjusted by the magnetic field between the neodymium magnet and the ferromagnetic core, which could be controlled by the plate gap distance. Therefore, the RM-TENG could independently power a commercial thermohygrometer sensor and 500 LEDs by its own operation.

Keywords Triboelectric nanogenerator · Multifunction · Rowing machine · Electrostatic discharge

1 Introduction

Triboelectric nanogenerators (TENG) are attracting attention as a promising energy-harvesting technology owing to their simple structure [1–4], low-cost fabrication [5–8], and applicability [9–11] for converting various mechanical motions such as pressing [12–14], sliding [15–17], and bending [18–20] into electrical energy. These advantages make TENGs well suited for self-sustaining systems such as wearable devices [21–24], sensing systems [25–28], and healthcare devices [29–31]. Consequently, many studies have explored designs that integrate TENGs into mechanical systems to harvest mechanical energy with minimum energy loss, which is rich in motion, including those involving human activity [32–34], vibration [35–37], and rotational dynamics [38, 39]. However, most TENG-integrated systems are designed to harvest mechanical energy and cannot be used as multifunctional components in such devices. Using such dual-function devices in these systems can improve the energy harvesting efficiency and enhance the utility of the system. However, most existing TENGs for human motion harvesting have limitations in terms of design complexity and reduced space efficiency. Therefore, such TENGs generate a low power output with low space efficiency and lack functionality, which limits their practical value. To overcome these limitations, it is necessary to study various design strategies in which the integrated systems contribute directly to the mechanical function of the original system rather than only being energy harvesters. Multifunctional energy harvesting components are required, particularly in the context of exercising equipment. This is

Jaeung Choi and Seh-Hoon Chung contributed equally to this work.

✉ Jinkee Hong
jinkee.hong@yonsei.ac.kr

✉ Sangmin Lee
slee98@cau.ac.kr

[1] School of Mechanical Engineering, Chung-Ang University, 84, Heukseok- ro, Dongjak-gu, Seoul 06974, Republic of Korea

[2] Center for Systems Biology, Massachusetts General Hospital, Harvard Medical School, Boston, MA 02114, USA

[3] Department of Chemical & Biomolecular Engineering, College of Engineering, Yonsei University, 50 Yonsei-ro, Seodaemun-gu, Seoul 03722, South Korea

because exercising equipment naturally involves continuous mechanical motion and demands adjustable resistance to optimize performance, enhance safety, and improve training outcomes. In addition, additional systems such as user exercise feedback system requires power source with energy harvesting and various sensors that can enhance usability. Therefore, for the commercialization of TENGs in exercise equipment, there is a need to study simple structures and efficient designs that combine high-performance energy harvesting with mechanical functionality.

In this study, we have examined a TENG-integrated multifunctional system designed for a rowing machine that can adjust the resistance and sensing signals using the magnetic attraction between a magnet and a ferromagnetic core. When rotational movement is performed with the rowing motion, the flexible films, including the dielectric films and metal films of the rotator, slide on the stator and generate an electrostatic discharge between the aluminum electrodes on the stator and the nickel electrode films on the rotator by the surface charge of the dielectric films. The RM-TENG then generated high voltage and current outputs of up to 440 V and 1.16 A, respectively. Mechanical resistance and additional electrical signals were generated by the neodymium magnets and ferromagnetic cores in this structure. Therefore, the RM-TENG can be operated as a multifunctional exercise machine that can harvest mechanical energy and provide controllable mechanical resistance and electrical signals to sense the rotational speed of a rotator.

2 Results

The overall structure and mechanism of the RM-TENG, including its key components, are shown in Fig. 1a–c. Figure 1a shows the overall structure of the RM-TENG. The RM-TENG is designed to generate electrical output, including if there is a gap between the two plates. This is because this device can also control the required force for exercise by the gap distance with magnetic force. Therefore, the RM-TENG can be separated into the stator and rotator parts. The stator is composed of bent films, such as two polyvinyl chloride (PVC) films, two nylon films, and four nickel fabric films on a polymethyl methacrylate (PMMA) substrate, for contact with the gap distance. The rotor was constructed

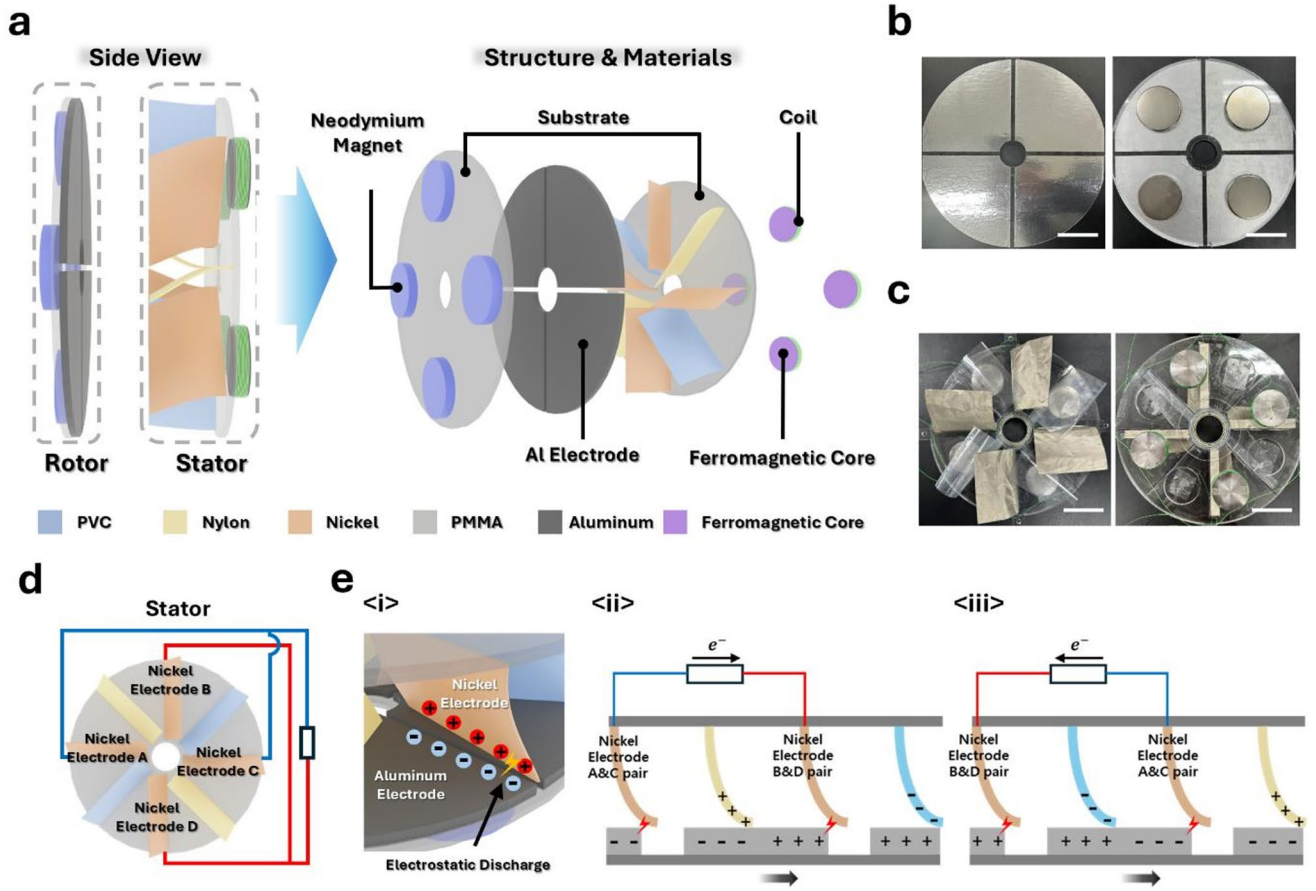


Fig. 1 Structure and mechanism of rowing machine-integrated multifunctional triboelectric nanogenerator (RM-TENG). (**a**) 3D structure and materials of RM-TENG. Photographs of front and back sides of (**b**) rotor and (**c**) stator. (Scale bar: 5 cm) (**d**) Electrical connection circuit of the stator. (**e**) Schematics of the discharge phenomenon and the electrical mechanism that occurs when the rotor of RM-TENG rotates

using a PMMA substrate and aluminum electrodes. The circuit is connected to nickel fabric films so that the electrical output can be generated by contact and separation between the aluminum electrodes and dielectric films. The neodymium magnets are located on the rotor, and the ferromagnetic cores are located on the stator. Therefore, the device can provide force for the exercise with magnetic force, and the required force can be managed by the disk gap distance. This magnetic force can generate electromagnetic electricity, which can provide further energy harvesting and various sensing capabilities.

Figure 1b and c show the photographs of front and back of rotor and stator, respectively, and Fig. 1d shows the detailed structure of the RM-TENG. The four nickel fabric electrodes in the stator were connected to generate electricity. Nickel electrodes A and C are connected to one terminal of the external circuit, whereas nickel electrodes B and D are connected to the opposite terminal. The detailed working mechanism of the RM-TENG is illustrated in Fig. 1e. As the PVC film contains negative surface charges and the nylon film contains positive surface charges, according to the triboelectric series [40], the charges inside the aluminum electrodes are polarized by the films of the stator. When the nickel electrodes were moved close to the aluminum electrodes, the polarized charges generated a high electric field between the aluminum and nickel electrodes. An electrostatic discharge was then generated between the two electrodes. As a result, the RM-TENG can generate a high electrical output based on electrostatic discharge, as shown in Fig. 1e-i. In addition, the proposed mechanism was verified through simulation. Figure S1 shows the COMSOL Multiphysics simulation results for the generation of the electric field between the nickel electrode and aluminum electrode. The geometry for this simulation result was set as same as RM-TENG, and the permittivity and surface charge density of the film was set as 2.1, and -7×10^{-6} C/m^2, respectively. The gap distance between the nickel electrode and aluminum electrode is set as 0.3 mm. The figure below shows the simulation result that calculated with COMSOL Multiphysics program. According to the simulation result, more than 3 kV/mm of electric field strength was generated between electrodes. As the breakdown voltage of dry air is about 3 kV/mm, this simulation result indicates that the RM-TENG can generate ESD based electrical output during the operation. Figure 1e-ii shows the electricity generation when the nylon film is in contact with the electrode, and Fig. 1e-iii shows the electricity generation when the PVC film is in contact with the electrode. When the nylon film contacts the aluminum electrode, the positive charges on the nylon film attract the negative charges inside the aluminum electrode. The positive charges are then polarized. The positive charges generate an electrostatic discharge to the nickel electrode when the nickel electrode approaches the aluminum electrode and generates an electrical output, as shown in Fig. 1e-ii. When the PVC film contacts with the aluminum electrode, the negative charges on the PVC film attract the positive charges inside the aluminum electrode. As the negative charges are polarized inside the aluminum electrode, an electrostatic discharge is generated in the opposite direction to the electrical current, as shown in Fig. 1e-iii. The RM-TENG can generate an electrical output based on the electrostatic discharge, while the rotator is rotated by the rotational force from the rowing machine.

Because the device generates electrical output by contact separation between the films and electrodes, various parameters influence the functionality of the RM-TENG. As shown in Fig. 2a, parameters such as the disk gap distance (W) (Fig. 2a-i), material selection for the dielectric films of stator (Fig. 2a-ii), and aluminum electrode segments of rotor (Fig. 2a-iii) were tested to optimize the structure of the RM-TENG. The disk gap distance is defined as the horizontal distance between the rotor and stator. Four fan-shaped aluminum electrodes with a central angle of 90 °each covered the PMMA substrate for the four segment electrode design. Two semicircular electrodes with a central angle of 180° each covered the PMMA substrate for the two segment design.

For the four dielectric films and four nickel fabric films, eight films were used at the top plate. The central angle of each segment of the bottom electrode influenced the electrical output. If the central angle of the electrode segments is larger than the angle between the nickel electrodes on the top plate, the opposite surface charges of the dielectric films can decrease the electrical output. When W decreases, the contact area between the dielectric films and the bottom electrodes increases because of film bending. The electrical output based on electrostatic induction can then be increased.

Figure 2b–e shows the experimental results for the voltage and current outputs with different W values and electrode segments at a rotation speed of 300 rpm to optimize the electrode design of the bottom plate and the effect of different gap distances. The peak voltage and current outputs of the two segments of the aluminum electrode-based RM-TENG with different disk gap distances are shown in Fig. 2b and c, respectively. No output was detected at a disk gap distance of 2 cm. Meanwhile, maximum peak voltages of approximately 64, 42, and 104 V were measured at gaps of 3, 4, and 5 cm, respectively. At a disk gap distance of 2 cm, no peak current was observed, whereas peak currents of 176, 232, and 128 mA were measured at 3, 4, and 5 cm, respectively. Figures 2d–e present the voltage and current outputs of the four segments of the aluminum electrode-based RM-TENG with different disk gap distances by giving

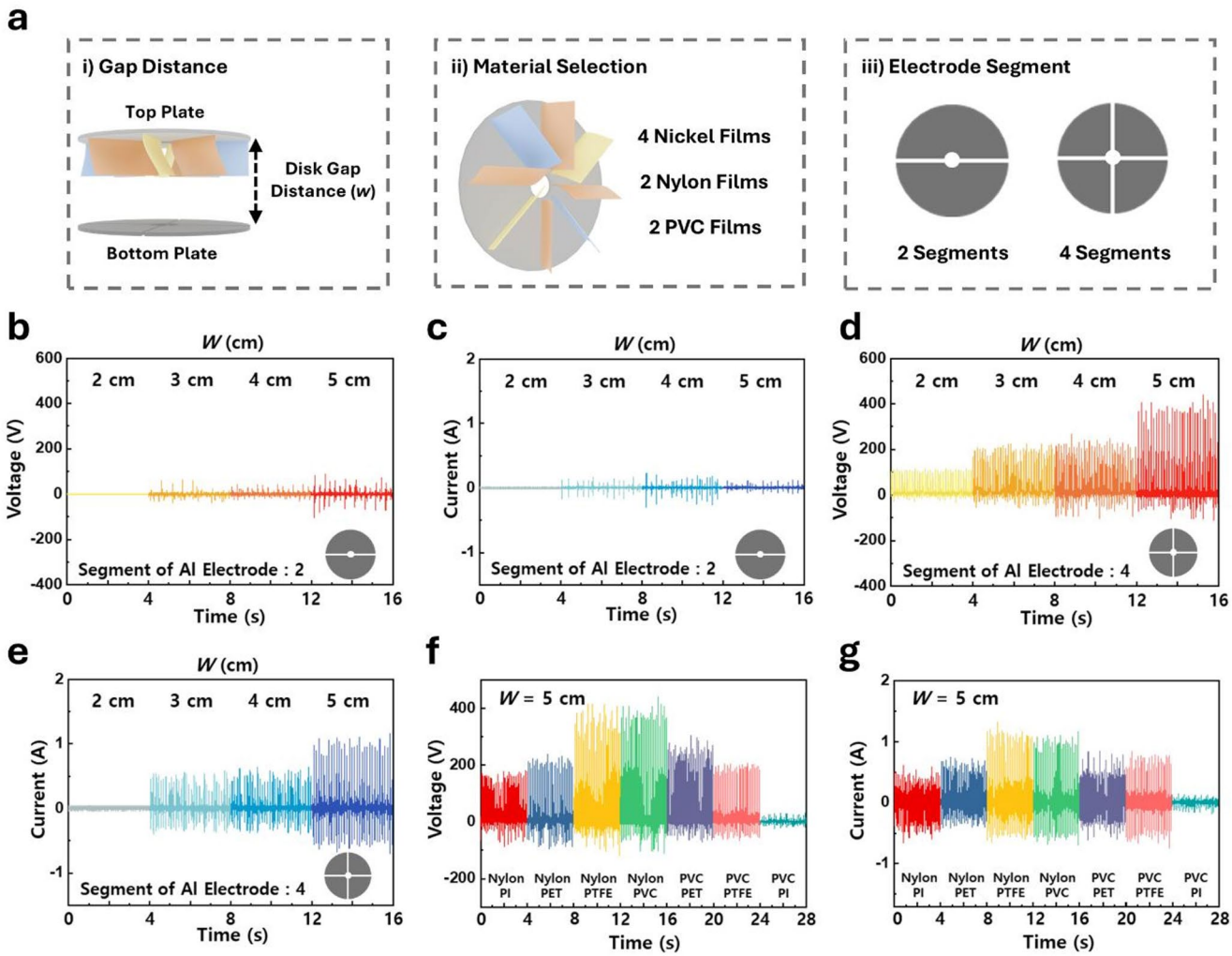


Fig. 2 Design variable experiment for RM-TENG (**a**) Visual description of variables (disk gap, material, aluminum electrode segment). (**b**) Voltage per disk gap (2, 3, 4, and 5 cm) when Al electrodes are two segments. (**c**) Current per disk gap (2, 3, 4, and 5 cm) when Al electrodes are two segments. (**d**) Voltage per disk gap (2, 3, 4, and 5 cm) when Al electrodes are four segments. (**e**) Current per disk gap (2, 3, 4, and 5 cm) when Al electrodes are four segments. (**f**) Voltage outputs according to the material of the stator. (**g**) Current outputs according to the material of the stator

a 300 RPM of rotational speed input. At a disk gap of 2 cm, the intrinsic elasticity of the film ensured a stable contact with the aluminum electrode, producing DC waveform outputs with measured voltages reaching approximately 100 V. In contrast, when the disk gap exceeded 3 cm, the stable interfacial contact enabled by the film's elasticity was lost. The breakdown voltage increased with an increase in the gap between the bottom plate and the bent films. According to Paschen's law, the air breakdown voltage depends on the gap distance between two metal electrodes. Therefore, the peak voltage output based on the electrostatic discharge can be increased by increasing the gap distance. Consequently, higher peak voltages and currents are generated with a larger W. At disk gaps of 3, 4, and 5 cm, the maximum peak voltages were measured at 224, 268, and 440 V, respectively, with the corresponding peak currents reaching 0.58, 0.64, and 1.16 A, respectively. Consequently, in the two-segment configuration, each segment is simultaneously swept by two electrically insulated nickel films, one PVC film, and one nylon film. The concurrent interaction of these materials in the same segment induces electrical interference, causing either the absence of output or isolated peak signals. However, when the electrode was divided into four segments, each segment was swept by a single nickel film and a single dielectric film (PVC or nylon). This eliminated the electrical interference observed in the two-segment case and allowed the generation of a stable discharge-type output. Therefore, the RM-TENG can generate a higher electrical output with the four electrode segments.

Because electrostatic discharge is generated by the surface charge of the dielectric films, the RM-TENG output can be influenced by material differences. To determine the

appropriate film materials for the RM-TENG, Fig. 2f–g show the voltage and current outputs of the RM-TENG with different dielectric films using nylon, polyimide (PI), polyethylene terephthalate (PET), polytetrafluoroethylene (PTFE), and PVC. A rotational speed of 300 rpm was used, and the gap distance between the top and bottom plates was 5 cm. According to Wang et al. [41, 42], these materials can contain more negative surface charges in the order of PVC > PTFE > PI > PET > Nylon. As PVC mostly contains negative surface charges, and nylon can contain positive surface charges, Fig. 2f–g show the electrical outputs with a combination of material pairs with nylon and PVC. When nylon was fixed and paired with PI, PET, and PTFE, the peak voltage and current were measured as 180 V and 0.62 A, 240, and 0.752 A, 416 V and 1.32 A, and 440 V and 1.16 A, respectively. When the PVC was fixed and paired with PET, PTFE, and PI, the peak voltage and current was measured up to 304 V and 0.84 A, 208 V and 0.84 A, and 32 V and 0.136 A, respectively. With the combination of nylon and PVC, the peak voltage and current output were measured as 440 V and 1.16 A, respectively. Consequently, the RM-TENG was optimized using nylon and PVC films to enhance electrical output. Furthermore, a durability test was conducted based on the optimized conditions. As shown in Figure S2, the voltage output was consistently maintained without any significant decreases throughout 120,000 cycles. Figure S3 shows a micrograph of the aluminum electrode taken before and after 120,000 cycles, revealing minor surface scratches that had no critical effect on the performance of the RM-TENG. Additionally, to evaluate the influence of humidity on the electrical output of the RM-TENG, the voltage output was measured under humidity conditions ranging from 22% to 55%. Although the voltage amplitude decreased with increasing humidity, electrostatic discharge was still observed, as shown in Figure S4. In addition, further studies for stable output of RM-TENG in high humid conditions is necessary.

To evaluate the accurate electrical performance of the RM-TENG, the voltage, current, and power were measured and calculated under various load resistances. The root mean square (RMS) values are shown in Figure S5, and the peak values are shown in Figure S6. The RMS voltage and current were obtained using the following equations:

$$RMS\ voltage = \sqrt{\frac{1}{T}\int V(t)^2 dt},\quad RMS\ current = \sqrt{\frac{1}{T}\int I(t)^2 dt}$$

where *V(t)* is the measured voltage output over time, *I(t)* is the measured current output over time, and *T* is the total time for measuring the voltage and current outputs.

The corresponding power values were calculated by multiplying voltage and current in each case. With a high load resistance, both voltage (RMS and peak) of the RM-TENG gradually increased, while the currents decreased. The highest RMS power output was calculated as 0.491 mW with 500 MΩ of load resistance. The highest peak power output was calculated as 94.5 W with 500 Ω of load resistance. The peak power output of RM-TENG was measured significantly higher than the RMS power due to the short duration of peak output of RM-TENG. As shown in Figure S7, the duration of one peak voltage output is only about 4 ms, thus there are empty intervals between each peak outputs. As a result, the peak power output could be measured higher than the RMS power which is also described in various previous references [43–45]. In addition, because the peak output of the RM-TENG was generated based on electrostatic discharge, the optimized peak power was measured with a lower load resistance, similar to the references for electrostatic discharge-based energy generators [46].

For multifunctional use of the RM-TENG, a neodymium magnet and ferromagnet were also used. This can provide additional force for exercise and electrical signals that can be used for force or rotational speed sensing and further energy harvesting. As shown in Fig. 3a and b, the attractive force between the neodymium magnet and the ferromagnet generates an additional force for rotation, which can provide the load force for the exercise. Because the attractive force is based on the magnetic force, this force can be controlled by *W*. Figure 3c shows the required torque for the RM-TENG with different *W*. When W was 2, 3, 4, and 5 cm, torques of 86.6 (SD : 4.7), 66.6 (SD : 4.7), 58.3 (SD : 4.3), and 49.2 (SD : 3.2) N·mm of torques were required, respectively. This indicates that the RM-TENG can provide further force for exercises based on its structure.

Because ferromagnets and neodymium magnets are used in the RM-TENG, it can also generate electrical output based on the electromagnetic electricity generation mechanism, as shown in Fig. 3d. When the RM-TENG rotates, the magnetic field from the neodymium magnet affects the ferromagnet and coil. Therefore, an electrical output can be generated. For the optimized electromagnetic output, Fig. 3e–f and Figures S8 and S9 show the electrical outputs with only the ferromagnetic core and the neodymium magnet, without any triboelectric effect, when the number of ferromagnetic cores is different. The voltage and current outputs of the devices that used two, four, and eight ferromagnetic cores with different *W* values are shown in Figure S8, Fig. 3e–f, and Figure S9, respectively. When two ferromagnetic cores were used, peak voltage outputs were generated up to 83.75, 71.6, 61.5, and 59 mV, and peak current outputs were generated up to 11.6, 9.2, 8, 7.6 mA, respectively. When four ferromagnetic cores are used, peak voltage outputs are generated up to 103.75, 78.15, 72.8, and 70.2 mV, respectively. Peak current outputs are generated up to 14, 10.4, 8.4, and

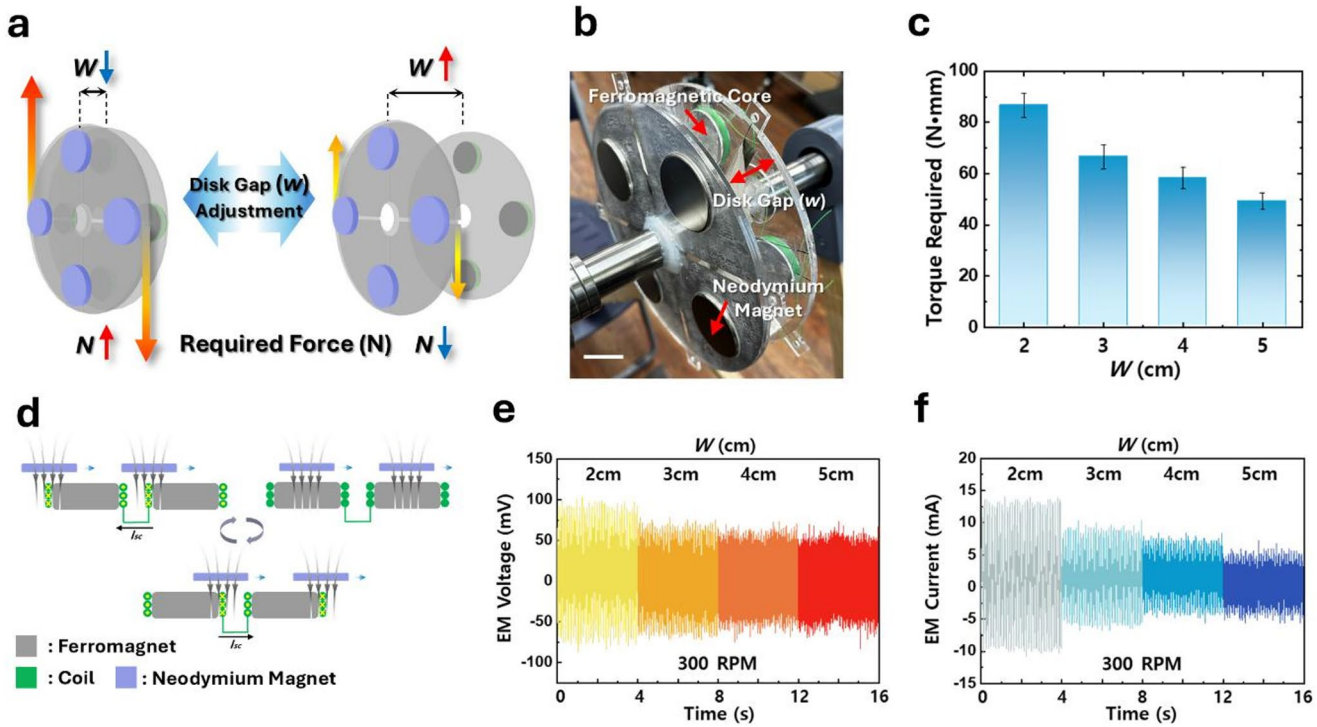


Fig. 3 Mechanical resistance control system and electrical output from electromagnetic induction. (**a**) 3D illustrates changes in mechanical resistance with disk gap. (**b**) Photograph of the fabricated RM-TENG. (Scale bar: 5 cm) (**c**) Minimum torque required for rotation according to disk gap. (**d**) Schematic illustration about the working mechanism of electromagnetic induction by ferromagnet and neodymium magnet. (**e–f**) Voltage and current outputs generated by electromagnetic induction according to disk gap (2, 3, 4, and 5 cm)

7.2 mA, respectively. When eight ferromagnetic cores were used, peak voltage outputs of up to 69.9, 69.5, 61.3, and 59 mV were generated, respectively, and peak current outputs of up to 7.2, 6, 6, 5.2 mA, respectively. The highest voltage and current outputs were generated with four ferromagnetic cores. Therefore, the device was optimized using four ferromagnetic cores with this structure.

With the electromagnetic output signal from the RM-TENG, as shown in Figure S10, the device has the potential to act as a rotational speed sensor during exercise. When W was fixed at 2 cm, different peak voltages and current outputs were generated at different rotational speeds. The peak voltages are generated up to 101.2, 96, and 77 mV, and the peak currents are generated up to 14, 11.6, and 9.2 mA when the rotational speed was 300, 240, and 180 RPM, respectively. For better analysis, the calibration curve of RMS voltage of EM output is shown in Figure S11. According to the fitting curve of Figure S11, the fitted regression equation was:

$$y = 0.0014 + 6.15766 \times 10^{-5}x$$

with an R-squared value was 0.9886. This indicates that the device can also operate as a self-powered rotational speed sensor when used as an exercise machine.

In addition, RM-TENG showed better voltage, current, peak power density, and durability than the existing TENGs for motion energy harvesting as shown in Table S1 [47–50]. This comparison shows that RM-TENG can generate significantly higher outputs with this electrostatic discharge based working mechanism with great durability.

Figure 4a illustrates the practical applications that can be operated with RM-TENG using TENG-based circuit designs for capacitor charging and LED powering. The charging circuit includes a rectifier, 4 mH inductor, electrolytic capacitor, and switch to efficiently store the peak output from the TENG [51, 52]. Similarly, the LED powering circuit had a simple design consisting of a rectifier, 500 LEDs, and a switch. In addition, to compare the output with only TENG output, only EM output, and both TENG and EM output, Figure S12 shows the charging graph 100 μF capacitor with only TENG output, only EM output, and both TENG and EM output. Accordingly, the TENG with EM output slightly charged the capacitor higher than only with TENG. And only with the EM output, lowest voltage was charged. This result indicates that the TENG is the primary power output of RM-TENG. Figure 4b shows the results of capacitor charging using the designed charging circuit. When the switch was turned on and the device was operated at 300 RPM for 200 s, electrolytic capacitors of

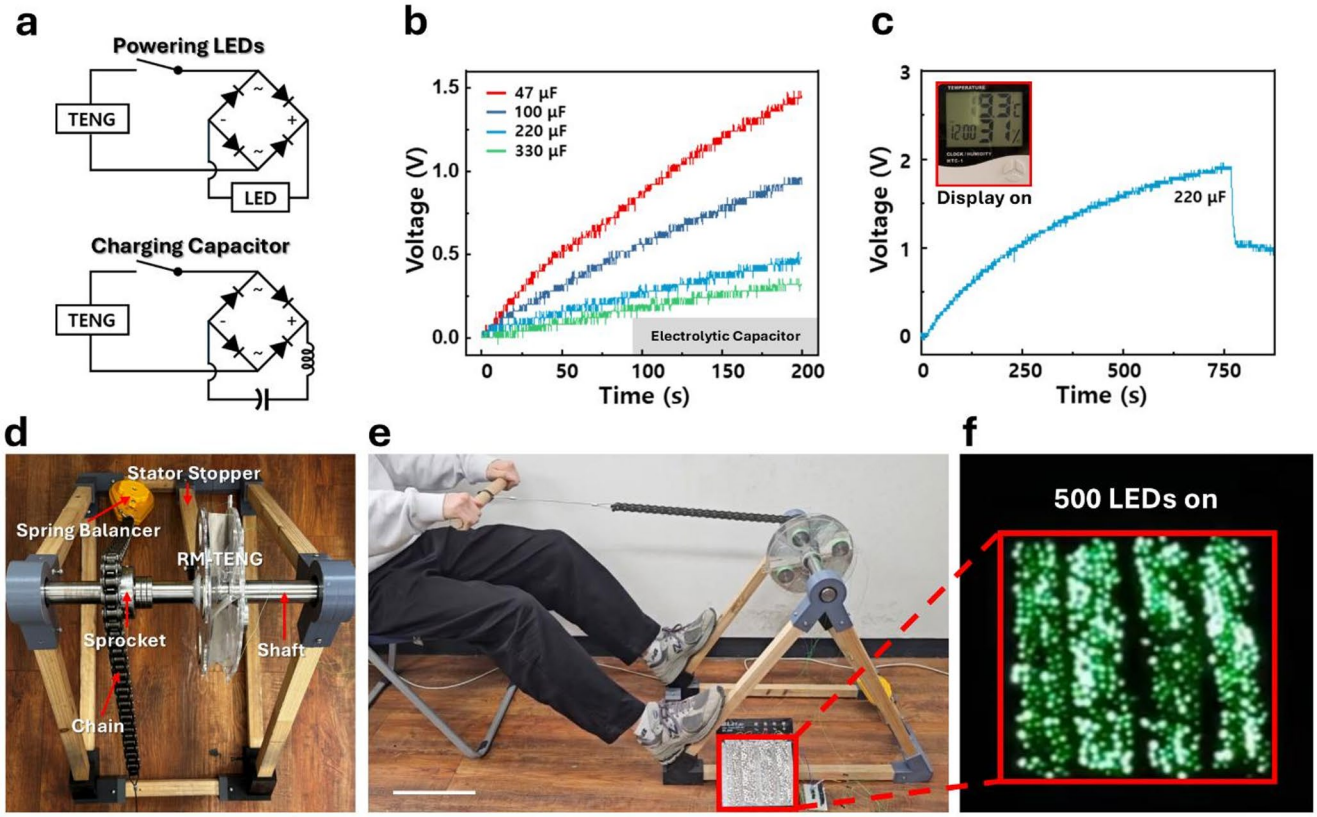


Fig. 4 Application demonstration of RM-TENG. (**a**) Circuit used for LED lighting and electrolytic capacitor charging. (**b**) Charging graph of the electrolyte capacitors (47, 100, 220, and 330 µF). (**c**) Commercial thermal-hygrometer sensor operation graph using 220 µF electrolytic capacitor. (**d**) Photograph of RM-TENG with descriptions of each components (**e**) Photograph of experimental setup for lighting 500 LEDs with RM-TENG. (Scale bar: 20 cm) (**f**) Photograph of powered LEDs with RM-TENG

47, 100, 220, and 330 µF were charged to 1.44, 0.96, 0.48, and 0.32 V, respectively. Charging the 220 µF electrolytic capacitor for 750 s with 300 RPM and 1200 s with 150 RPM successfully turned on the commercial thermohygrometer sensor, as shown in Fig. 4c and S13, respectively. In addition, the TENG was integrated into a rowing machine to demonstrate its practical applicability. Figure 4d shows the rowing machine structural components. The main structure, which was assembled from wooden beams and connectors, included a spring balancer, stator stopper, sprocket, chain, and shaft. Power is transmitted via a chain connected to a sprocket mounted on the shaft, and the spring balancer rewinds the extended chain. A bearing was installed at the center of the stator, which was locked using a stator stopper to restrict the rotational movement. The fabricated structure and experimental setup for powering the LEDs are shown in Fig. 4e and the circuit used to power the LEDs is shown in Fig. 4a. 500 LEDs were successfully powered by the RM-TENG during the exercise, as shown in Fig. 4f and Movie S1.

In addition, as RM-TENG generates ESD based electrical output, several hazards such as acoustic noise, ozone, and electromagnetic interference (EMI) could be concerned during operation. First, the acoustic noise of ESD was buried by the noise of rowing machine operation as shown in Movie S1. Second, according to the previous references [53, 54], more than 2 kV of ESD generated ozone, however, the voltage output was only measured up to 400 V, thus the side effect by the ozone is limited. Lastly, to analyze the EMI of ESD output, we measured RMS voltage values when EM was operated with TENG (V_a), when EM was operated only (V_b), and motor noise (V_c) as shown in Figure S14, and calculated signal-to-noise ratio (SNR) between the RMS value of EM output and TENG based noise output as follows:

$$V_{EM(rms)} = V_b - V_c = 32.71 - 14.13 = 18.58\,mV$$

$$\boldsymbol{V_{noise(rms)}} = V_a - V_b = 34.47 - 32.71 = 1.76\,mV$$

$$\frac{\boldsymbol{V_{EM(rms)}}}{\boldsymbol{V_{noise(rms)}}} = 10.6$$

The SNR of the EM signals was calculated using the following equation:

$$SNR_{dB} = 20\log_{10}\frac{V_{EM(rms)}}{V_{noise(rms)}}$$

$$SNR_{dB} = 20\log_{10}10.6 = 20.5\,dB$$

Based on the numerical results, the SNR was approximately 20.5 dB. This result shows that the EMI effect from ESD output of RM-TENG is limited.

3 Conclusion

In this study, we demonstrated a multifunctional RM-TENG by integrating a rowing machine and a TENG device that can generate a high electrical output based on electrostatic discharge and provide controllable mechanical load resistance and rotational speed sensing signals by low frictional movement. This design offers advantages such as reduced wear during high-speed rotation and the ability to control the resistance without complex mechanical components. The RM-TENG achieved a high peak output of approximately 440 V at 1.16 A without strong physical contact. Consequently, the RM-TENG successfully lit 500 LEDs through human-powered rowing motions using the fabricated rowing machine structure. It charged a 220 μF electrolytic capacitor and successfully operated a commercial thermos-hygrometer sensor. Although further research such as enhancing torque range with design optimization is necessary for commercial rowing machines, this study provides a foundation for future integration of TENGs into mechanical systems.

4 Methods

4.1 Fabrication of RM-TENG

The RM-TENG consists of a rotor and a stator. The rotor consists of neodymium magnet (Domagnet Co., Korea) and aluminum electrode based on round PMMA substrate (3 mm thickness, 200 mm in diameter). On one side of the PMMA substrate, the aluminum electrode was divided into four fan-shaped quarters. On the opposite surface of the PMMA substrate of the rotor, four neodymium magnets of 5 mm in thickness and 40 mm in diameter were symmetrically attached in a cross-shaped arrangement at 90-degree intervals, with all the magnets oriented to present the same magnetic pole outward. The stator consisted of eight films and a ferromagnetic core. The film consisted of two PVCs (thickness: 0.1 mm), two nylon films (thickness: 0.05 mm), and four nickel electrodes (thickness: 0.1 mm), and measured 75 mm in width and 60 mm in height. Four Ni electrodes were attached in a cross-shaped arrangement at 90-degree intervals. Triboelectric films composed of PVC and nylon were placed alternately between pairs of adjacent nickel electrodes at 45-degree intervals. These films were attached to the stator on the surface of the aluminum electrode of the rotor. Four ferromagnetic cores were attached in a cross-shaped arrangement at 90-degree intervals. Each ferromagnetic core was uniformly wrapped with 10 turns of copper wire.

4.2 Fabrication of Supporting Structure

The supporting structure includes the wooden beams, shaft, ball bearings, sprocket, spring balancer, chain, and joints connecting the wooden beams. The main framework was made of 30 × 30 mm cross-sectional wooden beams, and various joints were fabricated using a 3D printer (Ultimaker S7, Ultimaker Co., Netherlands). The shaft (30 mm in diameter), on which the rotor, stator, and sprocket were mounted, was installed in the upper joints of the wooden beam frame, where ball bearings were installed. A spring balancer connected to the chain, which returned the pulled chain, was installed at the lower part of the wooden beam frame, with the chain laid over the sprocket to enable smooth torque transmission. A one-way bearing was embedded inside the sprocket to ensure that the torque was transmitted only when the chain was pulled, while allowing free rotation in the opposite direction. The rotor was fixed to the shaft using an EVA adhesive and rotated together. A bearing is installed between the stator and shaft, and the stator is connected to an external structure called a stator stopper, which prevents it from rotating.

4.3 Characterization and Measurement

The voltage and current outputs were measured using a mixed-domain oscilloscope (MDO 34, Tektronix Co., USA) with differential probes (THDP0100, Tektronix Co., USA) and a current probe (TCP0030A, Tektronix Co., USA). For the parameter experiment, a brushless motor (BXM5120-GFS, Oriental Motor Co., Japan) combined with a motor driver (BXSD120-C2, Oriental Motor Co., Japan) was used to control the rotational speed.

Supplementary Information The online version contains supplementary material available at https://doi.org/10.1007/s40684-026-00847-z.

Acknowledgements This research was supported by the Chung-Ang University Graduate Research Scholarship in 2022. This work was supported by the National Research Foundation of Korea(NRF) grant, funded by the Korea government(MSIT) (Nos.2023R1A2C2006170, RS-2025-02214162).

Funding Open Access funding enabled and organized by Chung-Ang University

Data Availability The authors confirm that the data supporting the findings of this study are available within the article and its Supplementary material. Raw data that support the findings of this study are available from the corresponding author, upon reasonable request.

Declarations

Conflict of interest There are no conflicts of interest to declare.

Open Access This article is licensed under a Creative Commons Attribution 4.0 International License, which permits use, sharing, adaptation, distribution and reproduction in any medium or format, as long as you give appropriate credit to the original author(s) and the source, provide a link to the Creative Commons licence, and indicate if changes were made. The images or other third party material in this article are included in the article's Creative Commons licence, unless indicated otherwise in a credit line to the material. If material is not included in the article's Creative Commons licence and your intended use is not permitted by statutory regulation or exceeds the permitted use, you will need to obtain permission directly from the copyright holder. To view a copy of this licence, visit http://creativecommons.org/licenses/by/4.0/.

References

1. Wang, Y., Yang, Y., & Wang, Z. L. (2017). Triboelectric nanogenerators as flexible power sources. *Npj Flexible Electronics*, 1(1), 10.
2. Wang, Y., et al. (2025). Bending the straight into curved: A tree-ring-inspired fully printed omnidirectional triboelectric nanogenerator with ring-nested structure for all-in-one wearable self-powered systems and IoT smart packaging. *Nano Energy*, 135, 110631.
3. Moon, C.-J., et al. (2025). Enhanced performance of triboelectric nanogenerator based on TiO2 nanoparticle/Nylon 66 composite nanofibers. *International Journal of Precision Engineering and Manufacturing-Green Technology,* 13(1), 181–193. https://doi.org/10.1007/s40684-025-00736-x
4. Nguyen, D. C., et al. (2025). Field effect enhanced electric double layer for high-output droplet energy harvester. *Nano Energy*, 134, 110560.
5. Li, Y., et al. (2021). Low-cost, environmentally friendly, and high-performance triboelectric nanogenerator based on a common waste material. *ACS Applied Materials & Interfaces*, 13(26), 30776–30784.
6. Hu, S., et al. (2022). A Low-Cost simple sliding triboelectric nanogenerator for harvesting energy from human activities. *Advanced Materials Technologies*, 7(9), 2200186.
7. Pan, W., et al. (2025). Low-cost environmental-friendly strain sensor and triboelectric nanogenerator based on waste lyocell fabric. *Sensors and Actuators A: Physical*, *389,* 116541.
8. Son, J., et al. (2023). Recycled, Contaminated, crumpled aluminum Foil-Driven triboelectric nanogenerator. *Advanced Science*, *10*(28), 2301609.
9. Luo, J., & Wang, Z. L. (2020). Recent progress of triboelectric nanogenerators: From fundamental theory to practical applications. *EcoMat*, 2(4), e12059.
10. Yang, J., et al. (2025). Triboelectric nanogenerators with machine learning for internet of things. *Advanced Materials Technologies*, 10(4), 2400554.
11. Zhao, J., et al. (2021). Real-time and online lubricating oil condition monitoring enabled by triboelectric nanogenerator. *ACS Nano*, 15(7), 11869–11879.
12. Shao, J., et al. (2019). 3D mathematical model of contact-separation and single-electrode mode triboelectric nanogenerators. *Nano Energy*, 60, 630–640.
13. Guo, M., et al. (2025). Wearable pressure sensor based on triboelectric nanogenerator for information Encoding, gesture Recognition, and wireless Real-Time robot control. *Advanced Functional Materials*, 35(22), 2419209.
14. Min, G., et al. (2021). Origin of the contact force-dependent response of triboelectric nanogenerators. *Nano Energy*, 83, 105829.
15. Shao, J., et al. (2018). Studying about applied force and the output performance of sliding-mode triboelectric nanogenerators. *Nano Energy*, 48, 292–300.
16. He, W., et al. (2020). Boosting output performance of sliding mode triboelectric nanogenerator by charge space-accumulation effect. *Nature Communications*, 11(1), 4277.
17. Li, Z., et al. (2025). Crossing lateral-sliding type triboelectric nanogenerator. *Nano Energy*, 139, 110952.
18. Wang, L., et al. (2023). Wearable bending wireless sensing with autonomous wake-up by piezoelectric and triboelectric hybrid nanogenerator. *Nano Energy*, 112, 108504.
19. Liu, X., et al. (2025). Efficient triboelectric nanogenerators with on-demand auxetic structure achieving deformation matching in wearable devices. *Nano Energy*, 135, 110648.
20. Fan, J., et al. (2023). MXene supported by cotton fabric as electrode layer of triboelectric nanogenerators for flexible sensors. *Nano Energy*, 105, 107973.
21. Zou, Y., Raveendran, V., & Chen, J. (2020). Wearable triboelectric nanogenerators for Biomechanical energy harvesting. *Nano Energy*, 77, 105303.
22. Heo, D., et al. (2024). Self-powered emergency response gas-mask-system via multi-dielectric flutter with negligible inhalation resistance. *Chemical Engineering Journal*, 499, 156349.
23. Liu, Z., et al. (2019). Wearable and implantable triboelectric nanogenerators. *Advanced Functional Materials*, 29(20), 1808820.
24. Seung, W., et al. (2015). Nanopatterned textile-based wearable triboelectric nanogenerator. *ACS Nano*, 9(4), 3501–3509.
25. Xu, M., et al. (2019). A highly-sensitive wave sensor based on liquid-solid interfacing triboelectric nanogenerator for smart marine equipment. *Nano Energy*, 57, 574–580.
26. Yang, Y., et al. (2013). Human skin based triboelectric nanogenerators for harvesting Biomechanical energy and as self-powered active tactile sensor system. *ACS Nano*, 7(10), 9213–9222.
27. Pu, X., et al. (2017). Ultrastretchable, transparent triboelectric nanogenerator as electronic skin for Biomechanical energy harvesting and tactile sensing. *Science Advances*, 3(5), e1700015.
28. Du, Y., Wang, Z. L., & Wei, D. (2025). Emerging sensing systems based on triboelectric nanogenerator. *Nano Energy,* 111292. https://doi.org/10.1016/j.nanoen.2025.111292
29. Chen, X., et al. (2020). Advances in healthcare electronics enabled by triboelectric nanogenerators. *Advanced Functional Materials*, 30(43), 2004673.
30. Conta, G., et al. (2021). Triboelectric nanogenerators for therapeutic electrical stimulation. *Advanced Materials*, 33(26), 2007502.
31. Panda, S., et al. (2023). Sustainable solutions for oral health monitoring: Biowaste-derived triboelectric nanogenerator. *ACS Applied Materials & Interfaces*, 15(30), 36096–36106.
32. Hur, J., et al. (2025). Human-driven triboelectric nanogenerator via simultaneous harvesting of body-coupled energy. *Nano Energy*, 135, 110645.
33. Bai, P., et al. (2013). Integrated multilayered triboelectric nanogenerator for harvesting Biomechanical energy from human motions. *ACS Nano*, 7(4), 3713–3719.

34. Bhatia, D., et al. (2022). Triboelectric nanogenerator integrated Origami gravity support device for shoulder rehabilitation using exercise gaming. *Nano Energy*, 97, 107179.
35. Jung, Y., et al. (2020). Wire-based triboelectric resonator for a self-powered crack monitoring system. *Nano Energy*, 71, 104615.
36. Li, S., et al. (2020). A fully self-powered vibration monitoring system driven by dual-mode triboelectric nanogenerators. *Acs Nano*, 14(2), 2475–2482.
37. Chen, J., & Wang, Z. L. (2017). Reviving vibration energy harvesting and self-powered sensing by a triboelectric nanogenerator. *Joule*, 1(3), 480–521.
38. Cao, D. Q., et al. (2025). Self-powered and self-sensing water meter using contact-separation triboelectric nanogenerator with harvesting local head loss. *Journal of Water Process Engineering*, 72, 107397.
39. Lin, L., et al. (2013). Segmentally structured disk triboelectric nanogenerator for harvesting rotational mechanical energy. *Nano Letters*, 13(6), 2916–2923.
40. Zou, H., et al. (2019). Quantifying the triboelectric series. *Nature Communications*, 10(1), 1427.
41. Liu, D., et al. (2022). Standardized measurement of dielectric materials' intrinsic triboelectric charge density through the suppression of air breakdown. *Nature Communications*, 13(1), 6019.
42. Zhao, Z., et al. (2021). Selection rules of triboelectric materials for direct-current triboelectric nanogenerator. *Nature Communications*, 12(1), 4686.
43. Chung, J. (2019). *Ion-Enhanced Field Emission Triboelectric Nanogenerator* 9(37): 1901731.
44. Wu, J., et al. (2025). Managing the two mode outputs of triboelectric nanogenerators to reach a pulsed peak power density of 31 MW m − 2. *Energy & Environmental Science,* 18(5), 2381–2394.
45. Kim, D., et al. (2023). Mechanical spring discharge-based multipillar triboelectric nanogenerator with enhanced power output. *Nano Energy*, 107, 108130.
46. Chung, J., et al. (2019). Ion-enhanced field emission triboelectric nanogenerator. *Advanced Energy Materials*, 9(37), 1901731.
47. Zheng, Z., et al. (2024). High-performance all-textile triboelectric nanogenerator toward intelligent sports sensing and Biomechanical energy harvesting. *ACS Applied Materials & Interfaces*, 16(8), 10746–10755.
48. Son, J.-h, et al. (2022). Highly reliable triboelectric bicycle tire as self-powered bicycle safety light and pressure sensor. *Nano Energy,* 93, Article 106797.
49. Zhang, Z., et al. (2018). An air-cushion triboelectric nanogenerator integrated with stretchable electrode for human-motion energy harvesting and monitoring. *Nano Energy*, 53, 108–115.
50. Peng, F., et al. (2019). Facile fabrication of triboelectric nanogenerator based on low-cost thermoplastic polymeric fabrics for large-area energy harvesting and self-powered sensing. *Nano Energy*, 65, 104068.
51. Wang, Z., et al. (2021). Giant performance improvement of triboelectric nanogenerator systems achieved by matched inductor design. *Energy & Environmental Science*, 14(12), 6627–6637.
52. Chung, S. H., et al. (2025). Reaching new efficiency milestones in Low-Speed wind energy harvesting via noncontact stackable Ion-Gate-Based static discharge generator. *Advanced Energy Materials*, 15(21), 2500033.
53. Yulianto, E. (2019). *Power analysis of ozone generator for high capacity production*. in *Journal of Physics: Conference Series*. IOP Publishing.
54. Wei, L. S., et al. (2014). Experimental and theoretical study of Ozone generation in pulsed positive dielectric barrier discharge. *Vacuum*, 104, 61–64.

Publisher's Note Springer Nature remains neutral with regard to jurisdictional claims in published maps and institutional affiliations.

Jaeung Choi received B.S degree in mechanical engineering from Sunchon National University, Sunchon, South Korea in 2024. Currently, he is a master's degree candidate at the Chung-Ang University, Seoul, South Korea. His research interest includes triboelectric nanogenerators (TENGs), triboelectric sensors.

Seh-Hoon Chung received his B.S. in Engineering Mechanical & System Design Engineering from Hongik University, and his M.S in Mechanical Engineering from Chung-Ang University, South Korea, in 2020 and 2022, respectively. His research interests focus on the energy harvesting devices based on electrostatic discharge, and structure of wind generators.

Deokjae Heo received his B.S., M.S., and Ph.D. degrees in Mechanical Engineering from Chung-Ang University, South Korea, in 2018, 2020, and 2024, respectively. As of 2025, he is a postdoctoral researcher at Harvard Medical School. His research interests focus on the mechanical design of nanogenerators and nanobiosensors for energy harvesting and biomedical applications.

Sunghan Kim is an associate professor of School of Mechanical Engineering at Chung-Ang University. He received his Ph.D. degree in J. Mike Walker '66 Department of Mechanical Engineering at Texas A&M University in 2015. He worked as a postdoctoral fellow in School of Materials Science and Engineering at Georgia Institute of Technology from 2015 to 2017. His research interests lie in establishing essential design factors to optimize the tribological and mechanical properties of sustainable functional nanocomposites for biological, electrochemical, and mechanical applications.

Jinkee Hong is a Professor at Yonsei University in Seoul, South Korea. He received his Ph.D. in Chemical and Biological Engineering from Seoul National University in 2010 and completed postdoctoral training at the Massachusetts Institute of Technology (MIT) from 2010 to 2012 under the supervision of Prof. Paula T. Hammond. He previously held faculty positions at Chung-Ang University (School of Chemical Engineering and Materials Science) and Kyung Hee University (College of Natural Sciences), and established his independent research group in 2012. Professor Hong has authored over 327 peer-reviewed publications and has developed a strong international research program spanning biomaterials, polymeric nanomaterials, biointerfaces, and translational applications. His research group has been supported by numerous competitive research grants and industry-sponsored projects totaling several million U.S. dollars. His work focuses on engineering materials and interfaces for biologically and clinically relevant environments, with applications in biomedical and dental materials, antimicrobial and regenerative systems, and translational technologies. He was a Visiting Professor at Massachusetts General Hospital (Harvard Medical School) and a Visiting Professor in the Department of Mechanical Engineering at the Massachusetts Institute of Technology (MIT) during 2024–2025.

Sangmin Lee received his Ph.D. in Mechanical Engineering from Pohang University of Science and Technology (POSTECH) in 2011. Now he is a professor in the School of Mechanical Engineering at Chung-Ang University. His main research interests focus on the fields of Mechanical energy harvesting, Energy-loss harvesting, Triboelectric nanogenerator, Water electrification, Electrical stimulation, Energy transfer medium, Surface modification, and Kinematic design.